IMPLEMENTATION AND TESTING OF A NOVEL ROTOR DESIGN METHODOLOGY

N. A. Pissarski, D. Schröder, E. Stumpf
RWTH Aachen University, Institute of Aerospace Systems, 52062 Aachen, Germany

Abstract

A novel design methodology for rotors is presented, which enables inverse blade design based on a predefined radial bound circulation distribution, either according to a wind turbine regime (repeller) or a propeller regime. The methodology comprises a pair of algorithms for design and off-design computations that employ the vortex filament method (VFM) amid a combination of a prescribed wake model and lifting line theory (LLT). Particle image velocimetry (PIV) measurements are performed on exemplary rotor designs to validate the theoretically predicted circulation distributions. Experimental results are discussed under consideration of an extended VFM model containing a decambering correction and the conventional blade element momentum theory (BEMT) as a reference model. The methodology has applications in the design and analysis of rotors with a certain load distribution to enable the systematic modification of the local magnitude of the shedding vortex sheet in the rotor wake.

Keywords

propeller; wind turbine rotor; blade vortex interaction; vortex filament method

NOMENCLATURE

Formula symbols

a	axial induction coefficient	-
a'	tangential induction coefficient	-
B	number of blades	-
c	local chord length	m
C_d	drag coefficient	-
C_l	lift coefficient	-
C_n	normal force coefficient	-
C_t	tangential force coefficient	-
h	helical pitch	m
l	torsional parameter	m
Q	torque	N m
$\vec{e_r}$, $\vec{e_\theta}$, $\vec{e_z}$	basis vectors (cylindrical)	m
R	rotor radius	m
s	rotational direction parameter	-
t	regime parameter	-
T	thrust	N
u_i	induced velocity	m s^{-1}
u_iR	induced velocity rotor plane	m s^{-1}
U_0	free stream velocity	m s^{-1}
α	angle of incidence	rad
Γ_b	circulation of bound vortex	m^2 s^{-1}
Γ_tr	circulation of trailed vortex	m^2 s^{-1}
γ	pitch angle	rad
ϕ	local inflow angle	rad
Λ	aspect ratio	-
ρ	density	kg m^{-3}
σ	solidity ratio	-
Ω	angular velocity	rad s^{-1}

Abbreviations

BEMT	blade element momentum theory
BET	blade element theory
BVI	blade vortex interaction
EVFM	extended vortex filament method
FOV	field of view
LLT	lifting line theory
MT	momentum theory
PIV	particle image velocimetry
VFM	vortex filament method

doi: 10.25967/610516

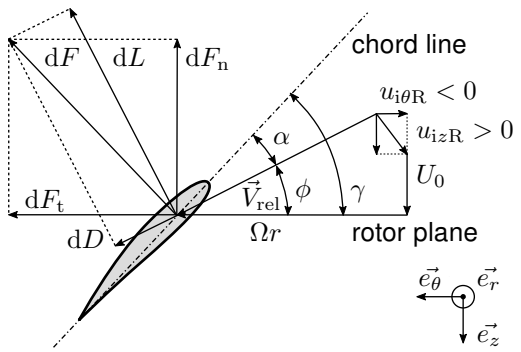

FIG 1. Velocity diagram and resulting fluid forces acting on a blade section in the propeller regime.

1. INTRODUCTION

The presence of a blade tip vortex system in rotor wakes disrupts the inflow of following blades in close proximity to the vortex sheet. This interaction between the concentrated tip vortex and the surface of the following blade causes the *blade vortex interaction* (BVI) phenomenon, which represents a major challenge due to its significant influence on, e.g., rotor noise emissions for rotary wing aircraft in hover conditions or slow flight [1], respectively accelerated fatigue damage for wind turbines [2]. To reduce the negative effects associated with BVI, new unconventional tip designs are investigated within the French-German research project TWIN-HELIX, which aim at splitting up the single tip vortex into a like-signed vortex pair [3] [4]. While being convected downstream, the vortex pair ultimately merges into a single vortex with a widened core radius and a decreased vorticity peak. Previous experimental measurements showed an unexpected rapid core growth prior to the onset of the merging process for several tip configurations. The physical origin of this behaviour is found in the presence of centrifugal instabilities, which are triggered when the radial circulation gradient changes sign with increasing distance from the vortex centre [5] [6] [7]. Following this approach, one hypothesis to explain the occurrence of this instability phenomenon is the accumulation of opposite-signed vorticity in the vicinity of the secondary vortex. The characteristics of this vorticity sheet behind the rotor blade are directly affected by the radial circulation distribution. Therefore, new rotor blades with predefined circulation distributions were required in order to investigate the effect of the shear layer on the centrifugal instabilities.
To allow not only the design of new rotor concepts but also the theoretical analysis of existing blade geometries, a novel design methodology was developed.

2. THEORETICAL MODELS ON ROTOR FLOW

The fundamental basis of general rotor theory is given by the *blade element theory* (BET), which represents the decomposition of the three-dimensional blade into individual blade elements of infinitesimal thickness [8]. This concept enables an idealised planar analysis of flow velocities and corresponding fluid forces acting on a blade element. Figure 1 shows the relevant parameters on an arbitrary blade segment.
If the velocity vector and hence the local angle of incidence (α) and inflow (ϕ) are known at each blade element, an evaluation and subsequent radial integration of the sectional normal and tangential force coefficient quantifies the thrust and torque of the entire blade. Hence, the determination of the velocity vector at each blade element constitutes the primary challenge in the rotor design process.
In analogy to two-dimensional profile theory, the normal (C_n) and tangential force coefficients (C_t) can be expressed as a function of the lift (C_l) and drag coefficients (C_d):

$$C_\mathrm{n} = C_\mathrm{l}\cos\phi - tC_\mathrm{d}\sin\phi\,, \tag{1}$$

$$C_\mathrm{t} = C_\mathrm{l}\sin\phi + tC_\mathrm{d}\cos\phi\,, \tag{2}$$

where the following notation is used to distinguish between a propeller and a wind turbine regime:

$$t = \begin{cases} +1 & \text{propeller regime} \\ -1 & \text{wind turbine regime}\,. \end{cases} \tag{3}$$

The angle of incidence $\alpha = t\,(\gamma - \phi)$ is dependent on the pitch angle (γ) and the angle of inflow. The latter may be formulated with regard to the decomposed velocity vector (see figure 1) as

$$\tan\phi = \frac{U_0 + u_{\mathrm{i}z\mathrm{R}}}{\Omega r + s u_{\mathrm{i}\theta\mathrm{R}}}\,, \tag{4}$$

where the direction of rotation is indicated using

$$s = \begin{cases} +1 & \text{negative rotation} \\ -1 & \text{positive rotation}\,. \end{cases} \tag{5}$$

The velocity vector consists of three components: the free stream velocity (U_0) of the rotor flow, the tangential velocity component (Ωr) and the vortex-induced velocity ($u_{\mathrm{i}z\mathrm{R}}$, $u_{\mathrm{i}\theta\mathrm{R}}$). A decomposition of the induced velocity vector yields the dimensionless quantities

$$a = t\frac{u_{\mathrm{i}z\mathrm{R}}}{U_0}\,, \tag{6}$$

$$a' = -st\frac{u_{\mathrm{i}\theta\mathrm{R}}}{\Omega r}\,, \tag{7}$$

namely the axial and tangential induction coefficients*. The computation of those velocities demands a wake model of adequate accuracy [9]. Two approaches for rotor wake modelling and fluiddynamic coupling between the wake and the rotor plane are presented below.

*The induction coefficients are defined to be predominantly positive along the blade.

2.1. Blade element momentum theory (BEMT)

An initial solution strategy to the rotor problem is based on the principle of linear and angular momentum conservation in the rotor flow, commonly considered as *momentum theory* (MT) and proposed as part of Glauert's *airscrew theory* [10]. This approach provides a general concept for the coupling of forces exerting on the rotor plane and the corresponding velocities in the wake in an annular control volume. Following Glauert's assumptions, the induced velocities can be obtained by equating the formulation of the azimuthally averaged thrust and torque in MT [8]

$$\frac{\mathrm{d}T}{\mathrm{d}r} = 4\pi\rho r U_0^2 a(1+ta)\,, \tag{8}$$

$$\frac{\mathrm{d}Q}{\mathrm{d}r} = 4\pi\rho r^3 \Omega U_0 a'(1+ta)\,, \tag{9}$$

and the corresponding formulations for thrust and torque from BET [8]

$$\frac{\mathrm{d}T}{\mathrm{d}r} = \frac{\rho c B U_0^2 (1+ta)^2}{2\sin^2\phi}\, C_\mathrm{n}\,, \tag{10}$$

$$\frac{\mathrm{d}Q}{\mathrm{d}r} = \frac{\rho c B U_0 (1+ta)\Omega r^2 (1-ta')}{2\sin\phi\cos\phi}\, C_\mathrm{t}\,. \tag{11}$$

The combination of MT and BET leads to a closed system of equations for the axial and tangential induction coefficient and is known as *blade element momentum theory* (BEMT) [8]:

$$a = \frac{1}{\frac{4F\sin^2\phi}{\sigma C_\mathrm{n}} - t}\,, \tag{12}$$

$$a' = \frac{1}{\frac{4F\sin\phi\cos\phi}{\sigma C_\mathrm{t}} + t}\,, \tag{13}$$

here, $\sigma = \frac{Bc}{2\pi r}$ defines the solidity ratio. The preceding equations of the BEMT are applicable to an arbitrary set of interindependent blade elements. The system of equations can therefore be solved for a single blade element without knowledge of another [8]. The assumption of azimuthally averaged and radially independent quantities is part of the MT as a solution strategy while representing a significant limitation of the BEMT. This limitation is evident when considering the difference between a rotor disc with an infinite and a finite number of blades [11]. In the latter case, Prandtl [12] demonstrates a decrease in circulation to zero level at the rotor blade tip, which stands in contrast to the finite limit given within BEMT [11]. Hence, the concept of tip loss was introduced and integrated into the BEMT model [10] [11]:

$$F = \frac{2}{\pi}\arccos\left[\exp\left(-\frac{B(R-r)}{2r\sin\phi}\right)\right]\,. \tag{14}$$

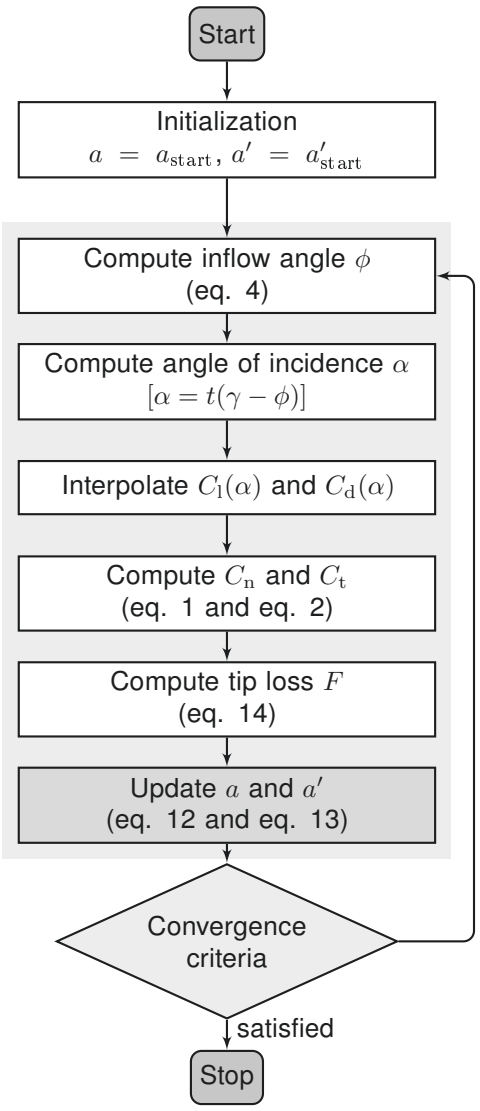

FIG 2. Flowchart of BEMT implementation applying a fixed point iteration technique.

The general BEMT equation system is nonlinear and implicit. Thus, a nonlinear solution technique or an iterative method is compulsive [8]. Figure 2 presents a flowchart of an exemplary BEMT algorithm, which uses a fixed point iteration technique and includes the tip loss factor.

2.2. Vortex filament method (VFM)

Another solution strategy to address the wake influence on the blade velocity vector is given within the *vortex filament method* (VFM), which employs potential theory as a conceptual basis. In principle, singularities in the form of potential vortices are introduced to the flow field, resulting in a local velocity field of finite circulation. The magnitude of vortex-induced circulation is proportional to the force per unit length perpendicular to the direction of the free stream velocity, as derived by Kutta and Joukowsky [13]:

$$F' = \rho U_0 \Gamma_\mathrm{b}\,. \tag{15}$$

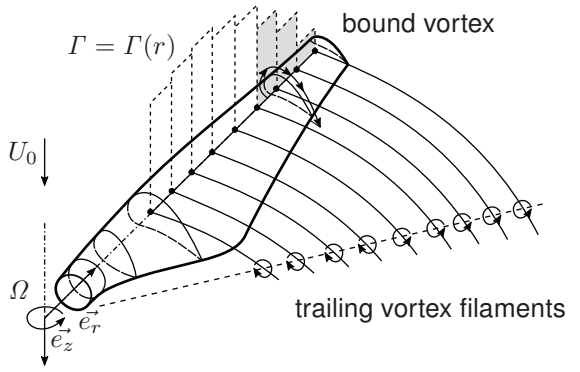

FIG 3. Radial bound circulation distribution and trailing vortices.

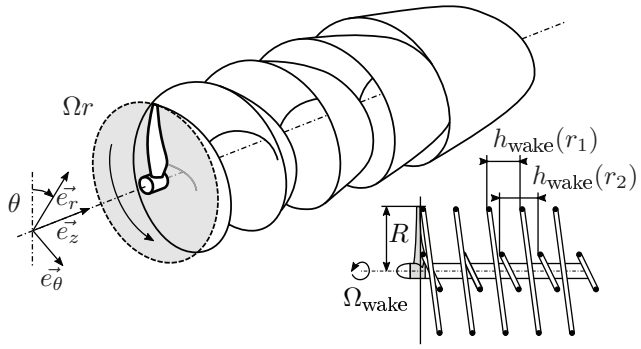

FIG 4. Vortex sheet composed of semi-infinite helical vortices.

Consequently, potential vortices are used to exert forces on, e.g., streamlined bodies with sharp trailing edges. These are known to be conform to the Kutta condition, which states the formation of a bound circulation (Γ_b) of sufficient strength to hold the rear stagnation point at the trailing edge, thus corresponding to physical observations [13].
In a similar manner, the rotor blade may be mathematically represented by a bound vortex of varying circulation within *lifting line theory* (LLT), corresponding to the work of Prandtl [12] (see figure 3). According to Helmholtz's first and second theorems, vortex lines are of constant strength and may not end in the fluid but must form a closed path [13]. Hence, an infinite number of vortices of strength

$$\Gamma_\mathrm{tr} = \frac{\mathrm{d}\Gamma_\mathrm{b}}{\mathrm{d}r}\,\mathrm{d}r \tag{16}$$

is shed from the trailing edge and convected downstream (see figure 3). In the present case of modelling rotor flow, it is reasonable to assume a vortex sheet composed of semi-infinite helical vortex filaments (see figure 4).
In combination with the formerly explained LLT, the VFM represents an accurate and computationally inexpensive method for solving the rotor problem when compared to results obtained from classical computational fluid dynamics [14] and experimental data [15].

The VFM comprises various approaches that can be divided into two categories: *free wake models* and *prescribed wake models*. Referring to a common prescribed wake model for rotor wakes that uses a set of non-congruent but rigid helices [16], the radially variable helical pitch (h_wake) and the angular velocity (Ω_wake) in the far wake represent the only degrees of freedom that need to be determined by relating the far wake and near wake parameters of the rotor flow (see figure 4). In analogy to equation 4 for computing the helical pitch in the rotor plane, a current relation for the helical pitch in the far wake is given as [17]

$$h_\mathrm{wake} = 2\pi r\,\tan\phi_\mathrm{wake} = 2\pi l\,, \tag{17}$$

$$\tan\phi_\mathrm{wake} = \frac{U_0 + \overline{u}_{\mathrm{i}z\mathrm{R}}}{\Omega r + s\overline{u}_{\mathrm{i}\theta\mathrm{R}}}\,, \tag{18}$$

where the torsional parameter (l) is introduced, and the angular velocity as well as the helical pitch are assumed to be the same in near wake and far wake conditions [17].
The induced velocities of an infinite helical vortex filament on the lifting line in the rotor plane can be found by applying an analytical formulation by Hardin [18]. The corresponding induced velocities of a semi-infinite helical vortex filament are determined by exploiting the symmetry of an infinite helix with respect to an arbitrary slicing plane perpendicular to the helical axis, dividing the helix into two semi-helices, and thus resulting in an induced velocity half the one obtained by an infinite helical vortex filament [19]. This leads to:

$$u_{\mathrm{i}z\mathrm{R}} = \tfrac{1}{2}\,u_{\mathrm{i}z,\,\mathrm{inf}} \quad \text{resp.} \quad \overline{u}_{\mathrm{i}z\mathrm{R}} = \tfrac{1}{2}\,\overline{u}_{\mathrm{i}z,\,\mathrm{inf}}\,, \tag{19}$$

$$u_{\mathrm{i}\theta\mathrm{R}} = \tfrac{1}{2}\,u_{\mathrm{i}\theta,\,\mathrm{inf}} \quad \text{resp.} \quad \overline{u}_{\mathrm{i}\theta\mathrm{R}} = \tfrac{1}{2}\,\overline{u}_{\mathrm{i}\theta,\,\mathrm{inf}}\,. \tag{20}$$

The exact analytical formulation found in Hardin [18] is based on modified Bessel functions. An approximate expression for infinite helical filaments is proposed by Okulov [20] in the following form:

$$\begin{aligned} &su_{\mathrm{i}z,\,\mathrm{inf}}(r,\,\chi) \\ &= +\frac{B\Gamma_\mathrm{tr}}{2\pi l}\left\{\begin{array}{c}1\\0\end{array}\right\} \\ &\quad + \frac{B\Gamma_\mathrm{tr}}{2\pi l}\,C_{0z}\left[\Re(\pm F_B) + \frac{1}{B}\,C_{1z}\Re(\log(1+F_B))\right], \end{aligned} \tag{21}$$

$$\begin{aligned} &u_{\mathrm{i}\theta,\,\mathrm{inf}}(r,\,\chi) \\ &= +\frac{B\Gamma_\mathrm{tr}}{2\pi r} - su_{\mathrm{i}z}\,\frac{l}{r}\,, \end{aligned} \tag{22}$$

where Γ_tr refers to the magnitude of circulation of a helical vortex filament at radius r_0, inducing a velocity $\vec{u_\mathrm{i}}$ at radius r. The upper value in curly braces applies for the condition $r < r_0$, whereas the lower value applies for $r > r_0$. F_B is defined as [20]

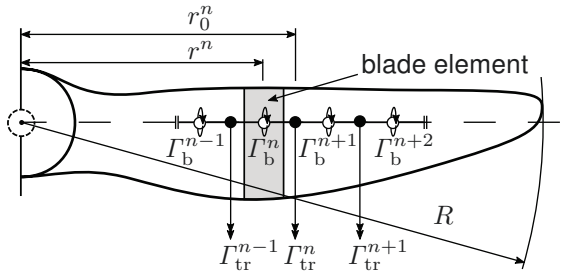

FIG 5. Piecewise constant discretization of the lifting line and corresponding indices.

$$F_B = \frac{1}{\mathrm{e}^{\mp B\xi - iB\chi} - 1}\,, \tag{23}$$

where e^{ξ} is given as [20]

$$\mathrm{e}^{\xi} = \frac{r}{r_0}\frac{\left(l + \sqrt{l^2 + r_0^2}\right)\exp\left(\sqrt{l^2 + r^2}/l\right)}{\left(l + \sqrt{l^2 + r^2}\right)\exp\left(\sqrt{l^2 + r_0^2}/l\right)}\,. \tag{24}$$

The definitions of the remaining variables are expressed in the form of Lerbs [21]:

$$C_{0z} = \left(\frac{l^2 + r_0^2}{l^2 + r^2}\right)^{\frac{1}{4}}\,, \tag{25}$$

$$C_{1z} = \frac{l}{24}\left[\frac{9r_0^2 + 2l^2}{(l^2 + r_0^2)^{\frac{3}{2}}} + \frac{3r^2 - 2l^2}{(l^2 + r^2)^{\frac{3}{2}}}\right]\,. \tag{26}$$

To determine the radially variable helical pitch, the analysis is carried out in the rotor far wake by employing an infinite helical vortex filament and computing the azimuthally averaged induced velocities on the basis of the Hardin formulation [18] given as

$$\overline{u}_{\mathrm{i}z}(r) = \frac{1}{2\pi}\int_0^{2\pi} u_{\mathrm{i}z}(r,\,\chi)\mathrm{d}\chi = \frac{sB\Gamma_t}{2\pi l}\quad\left\{\begin{array}{c}1\\0\end{array}\right\}\,, \tag{27}$$

$$\overline{u}_{\mathrm{i}\theta}(r) = \frac{1}{2\pi}\int_0^{2\pi} u_{\mathrm{i}\theta}(r,\,\chi)\mathrm{d}\chi = \frac{B\Gamma_t}{2\pi r}\quad\left\{\begin{array}{c}0\\1\end{array}\right\}\,. \tag{28}$$

The implementation of VFM requires a discretization of the formerly assumed continuous radial circulation distribution of the bound vortex (see figure 5). Therefore, a total of N equally distributed control points are introduced along the lifting line between the hub radius r^1 and the tip radius r^n. Hereafter, the superscript index number corresponds to the associated control point index for discretized formulae (see figure 5). A number of $N-1$ helical vortex filaments of strength

$$\Gamma_\mathrm{tr}^n = \Gamma_\mathrm{b}^{n+1} - \Gamma_\mathrm{b}^n \tag{29}$$

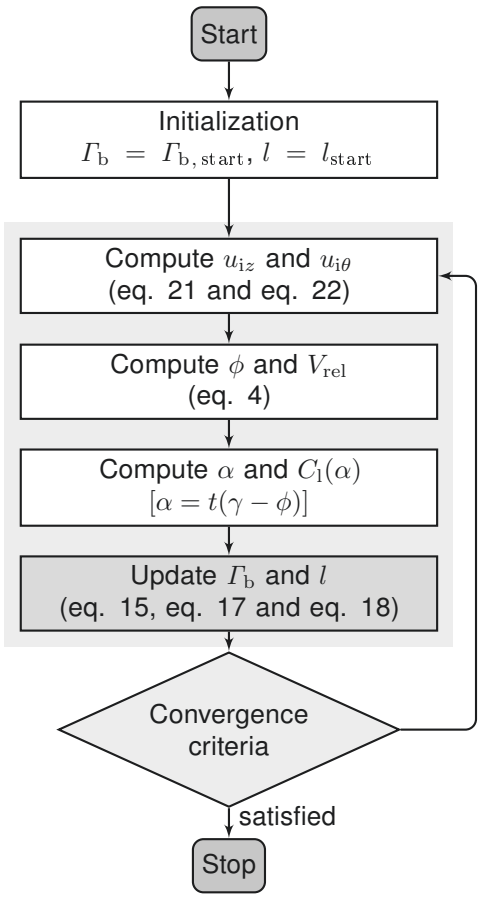

FIG 6. Flowchart of VFM-LLT implementation applying a fixed point iteration technique.

are shed from the midpoint of two consecutive control points at radius r_0^n. In its discretized form, the VFM system of equations is evaluated at each control point. Hence, it is necessary to define the azimuthally averaged induced velocities for the determination of the helical pitch (equation 18) at radius r_0^n by applying the arithmetic mean of two consecutive control points. Iteration is again compulsive to solve the system of nonlinear and implicit VFM equations. Figure 6 provides the flowchart of the imlemented VFM in terms of a lifting line rotor model and a fixed point iteration technique.

2.3. Extended vortex filament method (EVFM) with decambering model

A limitation of LLT is present considering the neglected chordwise expansion of the blade. Taking into account the existence of vortex-induced velocities perpendicular to the virtual chord line and thus an additional negative camber of the airfoil, the loading in the tip blade section is found to be overestimated [22]. A correction model to the *decambering effect* applying thin airfoil theory is proposed by Soerensen et al. [22] given as

$$\Delta\Gamma_{\mathrm{b},\,j} = \frac{\Delta\theta c_j}{\cos\alpha_j}\sum_{k=1}^{M}\left(w_{jk} - w_{j,\,\frac{1}{4}}\right)(\cos\theta_k - 1)\,, \tag{30}$$

where $w_{jk} - w_{j,\,\frac{1}{4}}$ denotes the difference between the vortex-induced velocity perpendicular to the chord line at a specified position and the vortex-induced velocity at the quarter chord line. A number of M evaluation points following a cosine distribution given as

$$x_k = \frac{c}{2}\,(1 - \cos\theta_k) \tag{31}$$

is placed along the chord of the blade at the corresponding angle

$$\theta_k = \pi \frac{k-1}{M-1}\,, \quad k \in [1,\, M]\ . \tag{32}$$

The exploitation of helical symmetry in equations 19 and 20 limits the determination of the vortex-induced velocity to the lifting line in the rotor plane within the conventional VFM model, considering a semi-infinite helical vortex filament [19]. It is therefore compulsive to replace the vortex filaments with a helical mesh of polygons, where each polygon edge represents a straight vortex filament, thus generating a mesh of elementary vortices [23]. The application of Biot-Savarts law to a straight vortex filament of finite length yields [24]

$$\vec{u}_{\Gamma_{\mathrm{tr}}}(\vec{x}) = \frac{\Gamma_{\mathrm{tr}}}{4\pi}\,\frac{(r_1 + r_2)(\vec{r}_1 \times \vec{r}_2)}{r_1 r_2 (r_1 r_2 + \vec{r}_1 \cdot \vec{r}_2)}\ . \tag{33}$$

In the context of this contribution, the prementioned model is referred to as *extended vortex filament model* (EVFM).

3. DESIGN METHODOLOGY

The design methodology covers design and off-design computations that employ a prescribed wake model within VFM in combination with LLT. The workflow is presented in figure 7. Prior to the design computation, flow and rotor geometric parameters, along with the targeted spanwise circulation distribution, are to be defined, whereas one geometric parameter remains unassigned, representing a degree of freedom. In terms of the geometric parameters, the definition of the blade geometry in the design process requires the specification of sectional airfoils, pitch angle, and chord length. The latter is determined with a VFM inverse design method that is presented below. Airfoils and chord length distribution are specified in advance. The resulting rotor blade is geometrically and aerodynamically twisted. It is not required to provide a specific airfoil geometry at each blade element since a seamless blade geometry is obtained by applying an interpolation method between defined cross sections. Sectional airfoil data in terms of lift and drag coefficient is generated utilizing the panel-based method XFOIL [25] and corrected as proposed by Snel et al. [26] to account for rotational effects (see section 3.2). Within the process, a lower threshold value of the Reynolds number of 25 000 is taken into account in the presented case [27]. Off-design analysis on the basis of VFM and a hub correction model (see section 3.2) enables a subsequent investigation on the influence of the flow parameters.

3.1. VFM inverse design method

To determine the pitch angle corresponding to a predefined radial circulation distribution, a VFM inverse design method is employed, which is in exact consistency with the VFM analysis formulation. A superposition of the azimuthally averaged induced velocities of $N-1$ helical vortex filaments at control point n yields the resulting induced velocities

$$\overline{u}_{\mathrm{i}z}(r^n) = \overline{u}^n_{\mathrm{i}z} = \frac{sB}{2\pi} \sum_{i=n}^{N-1} \frac{\Gamma^i_{\mathrm{tr}}}{l^i} \qquad \forall\, n \in \{2, \ldots, N-1\}\,, \tag{34}$$

$$\overline{u}_{\mathrm{i}\theta}(r^n) = \overline{u}^n_{\mathrm{i}\theta} = \frac{B}{2\pi r^n} \sum_{i=1}^{n-1} \Gamma^i_{\mathrm{tr}} \qquad \forall\, n \in \{2, \ldots, N-1\}\,. \tag{35}$$

The boundary values are set to $\overline{u}^1_{\mathrm{i}z}, \overline{u}^N_{\mathrm{i}z} = 0$ and $\overline{u}^1_{\mathrm{i}\theta}, \overline{u}^N_{\mathrm{i}\theta} = 0$. The azimuthally averaged induced velocity at the origin of a helical vortex filament on the lifting line at radius r^n_0 is defined as the arithmetic mean of two consecutive control points

$$\begin{aligned} \overline{u}^n_{\mathrm{i}z,\,\mathrm{m}} &= \frac{\overline{u}^n_{\mathrm{i}z} + \overline{u}^{n+1}_{\mathrm{i}z}}{2} \\ &= \frac{sB}{4\pi}\left[2\left[\sum_{i=n}^{N-1} \frac{\Gamma^i_{\mathrm{tr}}}{l^i}\right] - \frac{\Gamma^n_{\mathrm{tr}}}{l^n}\right]\,, \end{aligned} \tag{36}$$

$$\begin{aligned} \overline{u}^n_{\mathrm{i}\theta,\,\mathrm{m}} &= \frac{\overline{u}^n_{\mathrm{i}\theta} + \overline{u}^{n+1}_{\mathrm{i}\theta}}{2} \\ &= \frac{B}{4\pi}\left[\left(\frac{1}{r^n} + \frac{1}{r^{n+1}}\right)\left[\sum_{i=1}^{n-1} \Gamma^i_{\mathrm{tr}}\right] + \frac{1}{r^{n+1}}\Gamma^n_{\mathrm{tr}}\right]\,. \end{aligned} \tag{37}$$

The far wake helical pitch angle is available as a function of the induced velocities (equation 18). Insertion of the respective azimuthally averaged induced velocities in regard to the symmetry conditions equations 19 and 20 and the definition of the torsional parameter (equation 17) provides a residual function

$$\mathcal{R}^n(l) = l^n - r^n_0\,\frac{U_0 + \frac{1}{2}\,\overline{u}^n_{\mathrm{i}z,\,\mathrm{m}}(l)}{\Omega r^n_0 + \frac{1}{2}\,s\overline{u}^n_{\mathrm{i}\theta,\,\mathrm{m}}} \tag{38}$$

being solely dependent on the torsional parameter vector (l). The torsional parameter vector is determined by the application of the Newton-Raphson method based on a Jacobian matrix of upper triangular form

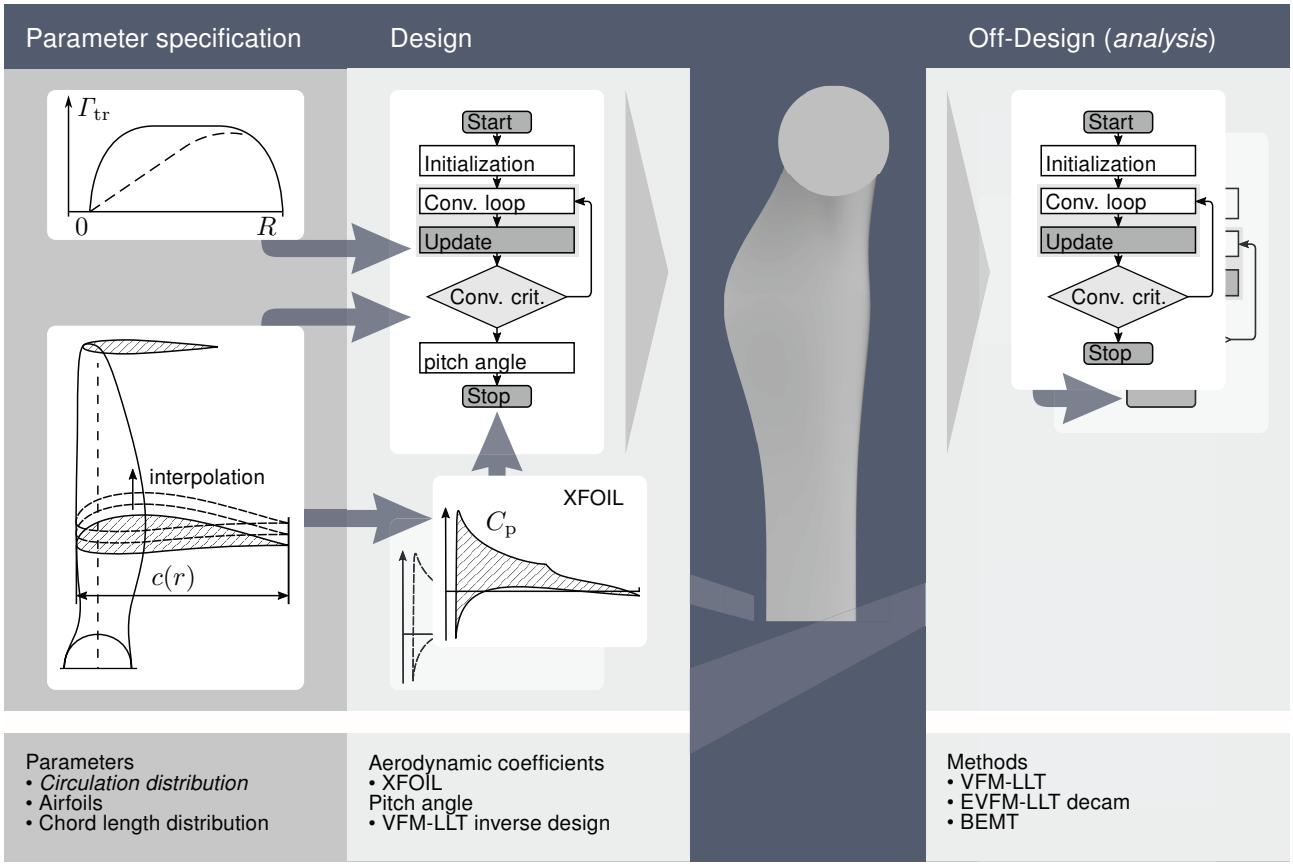

FIG 7. Inverse design methodology for rotors.

(39)

$$\mathcal{J}_{\mathcal{R}}(l) = \frac{\partial \mathcal{R}^i}{\partial l^j}(l) = \begin{pmatrix} \frac{\partial \mathcal{R}^1}{\partial l^1} & \frac{\partial \mathcal{R}^1}{\partial l^2} & \cdots & \frac{\partial \mathcal{R}^1}{\partial l^{N-1}} \\ \frac{\partial \mathcal{R}^2}{\partial l^2} & \cdots & \frac{\partial \mathcal{R}^2}{\partial l^{N-1}} \\ 0 & \ddots & \vdots \\ & & \frac{\partial \mathcal{R}^{N-1}}{\partial l^{N-1}} \end{pmatrix},$$

where the partial derivatives are formulated as

(40)

$$\frac{\partial \mathcal{R}^i}{\partial l^j}(l) = 1 - r_0^i \frac{\frac{1}{2}\frac{\partial \overline{u}^i_{\mathrm{iz,m}}}{\partial l^j}(l)}{\Omega r_0^i + s\overline{u}^i_{\mathrm{i}\theta,\mathrm{m}}}$$

The problem is solved by iterative evaluation of the Jacobian matrix with respect to the iteration specification

(41)

$$\mathcal{J}_{\mathcal{R}}(l_n)\Delta l_n = -\mathcal{R}(l_n)\,,$$

(42)

$$l_{n+1} = l_n + \Delta l_n\,,$$

where the subscript index number corresponds to the iteration step. Figure 8 illustrates the algorithm.

3.2. Adaptation and correction

The design methodology provides three correction models to adapt the initially calculated pitch angles in close proximity to the rotor hub and blade tip. In the first case, it is addressed that the application of the VFM inverse design method generally produces a result that is impractical in the rotor hub and transition section (see figure 9) due to the required connection between the blade and the shaft. Further, the method is sensitive due to the obligatory steep decline of the spanwise bound circulation in the area of the blade tip, leading to considerable pitch angle gradients that are not applicable. The spanwise pitch angle curve is therefore adapted in the prementioned regions (see figure 9) based on an extrapolation of the provided pitch angle in the main blade section.

As a second correction model, a modification to the rotor flow model at the rotor hub is introduced to include an approximate wall boundary condition. With respect to this condition, the rotor hub is represented as a contour flow surface in the form of an infinite cylindrical surface in a potential-theoretical model as proposed by Kerwin et al. [28]. Hence, the elimination of the radial component of the velocity perpendicular to the cylindrical surface is inherent in the definition. The resulting flow is modelled approximately using image vortices of magnitude $\Gamma_{\mathrm{tr},2} = -\Gamma_{\mathrm{tr},1}$ and of identical helical pitch, referring to the original vortex at the radial position

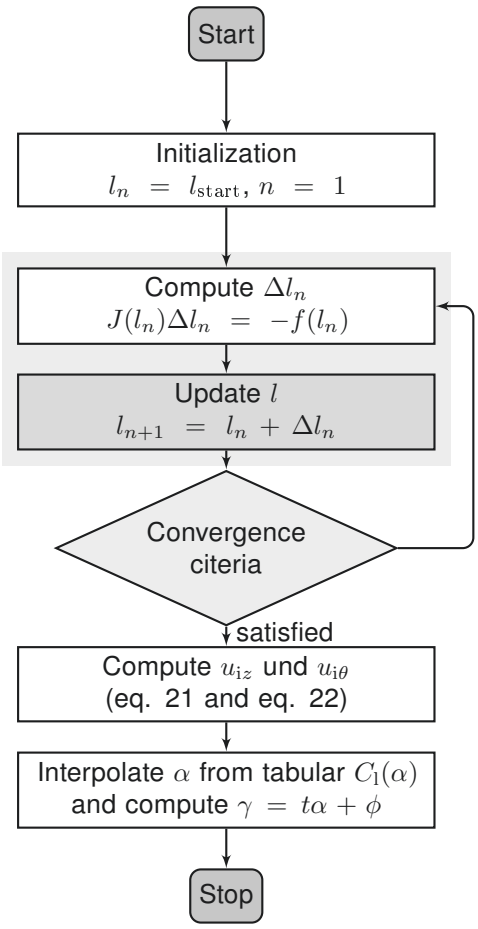

FIG 8. Flowchart of the VFM-LLT inverse design methodology.

$$r_2 = \frac{r_{\text{hub}}^2}{r_1}\,. \tag{43}$$

Here, r_{hub} defines the radius of the rotor hub [28]. The approximation is valid for sufficiently large helical pitch values [29]. It has to be noted that the influence of image-vortex-induced velocities is neglected in equations 34 and 35 for reasons of a clear presentation of the method.

A third correction model is available to account for centrifugal and Coriolis effects. Similarity considerations within the work of Snel et al. [30] demonstrate an increase in lift with ascending levels of the dimensionless ratio $\frac{c}{r}$, respectively, the local solidity ratio of the blade (σ). A general approach to compensating for rotational effects is given in the form of

$$C_{\bullet\,\text{rot}} = C_{\bullet\,\text{non-rot}} + f_\bullet \left(C_{\bullet\,\text{pot}} - C_{\bullet\,\text{non-rot}}\right) \tag{44}$$

where $\bullet$ replaces the indices l or d [19]. The coefficient $f_\bullet$ is set as proposed by Lindenburg [31] [32], Du et al. [33], or Chaviaropoulos et al. [34], alternatively Snel et al. [26]. With regard to the last-mentioned model,

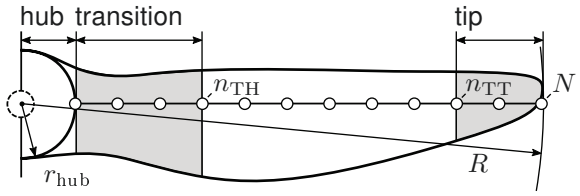

FIG 9. Partitioning of the rotor blade into functional areas: hub, transition, main, and tip sections.

$$f_{\mathrm{l}} = 3\left(\frac{c}{r}\right)^2\,, \tag{45}$$

$$f_{\mathrm{d}} = 0\,, \tag{46}$$

are defined derived from an empirical fit [31]. This model is chosen for all further calculations in the context of this contribution due to its low complexity. The airfoil performance for large angles of incidence is approximated on the basis of the flat plate model [19].

4. EXPERIMENTAL INVESTIGATION

To validate the introduced design methodology, two single-bladed rotors of different aspect ratios (Λ) were investigated within the propeller regime under constant inflow conditions and at identical tip-chord-based Reynolds numbers. The design objective in both cases was to achieve a mainly constant circulation distribution in spanwise direction. Experiments were carried out in a closed circuit water tunnel with a test section that measures 1.5 m in width, 1 m in height, and 6.5 m in length at an inflow velocity of 0.114 m s^{-1} thus preventing recirculation regions in the blade tip area in near-hover conditions.

4.1. Rotor geometry

For the first blade design, the following geometric constraints are established: The blade chord is kept constant at 80 mm, and the maximum blade radius is limited to 240 mm. The second blade design has a variable chord. It decreases from a maximum length of 85 mm towards a tip chord length of 50 mm. The rotor radius of the second blade is increased to 260 mm, thus increasing the blade aspect ratio, which constitutes an improved approximation to the lifting line model. Figure 10 shows the chord (solid lines) and the corresponding pitch angles (dashed lines) for both blade designs. Given the boundary condition of an identical tip Reynolds number of 120 000 ($\mathrm{Re} = \frac{\Omega R c}{\nu}$), the corresponding rotation rate is set to $f_1 = 1.00$ Hz and $f_2 = 1.47$ Hz, respectively. The pitch angle is determined by the proposed VFM inverse design method to meet the design requirement of a mainly constant circulation distribution using a radial discretization of the rotor blade with 40 blade elements. Hence, improved lift performance is needed near the rotor hub, and thus,

TAB 1. Flow and geometric design parameters of both rotor configurations

	Blade I	Blade II
R [mm]	240	260
c [mm]	80	85 . . . 50
Λ	3.00	3.80
f [Hz]	1.00	1.47
U_0 [m s^{-1}]	0.114	0.114
Re	120 000	120 000

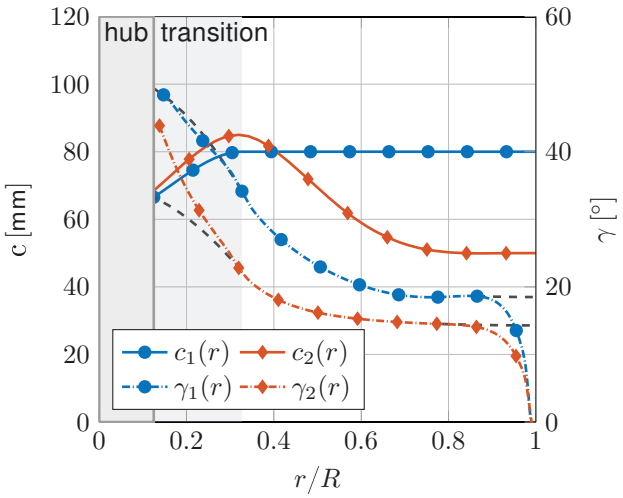

FIG 10. Comparison of the radial pitch angle and chord length for both blade designs. The extrapolated radial pitch angle curve is indicated in black.

in a region of low effective velocities, a low Reynolds number airfoil (SD7062) is employed, whereas a symmetrical airfoil (NACA0012) is utilized in the region of high effective velocities near the rotor tip. Aerodynamic twisting along the span of the rotor blade is achieved by interpolation of cross sections in between the outer airfoils. Manufacturing of the rotor blades is carried out using stereolithography in a rapid prototyping process. Table 1 provides an overview of the geometric specifications and experimental conditions used for both blades. Schematics of the determined blade geometries are presented in figure 11. The VFM method was applied in the grey regions, whereas the hub connection and the tip of the blade are characterised by geometric constraints as outlined in section 3.2. The corresponding extrapolated radial pitch angle curve is shown in black in Figure 10.

4.2. PIV measurements

The computation of the spanwise circulation distribution is accomplished through investigation of the vortex sheet in a two-dimensional plane close behind the trailing edge, as an investigation in the Trefftz plane is not possible due to dissipational effects. The vorticity magnitude is obtained as the curl of the two-dimensional velocity field, where the vorticity component perpendicular to the prementioned plane represents a scalar field. The spanwise circulation distribution is subsequently determined as the chordwise integral of the scalar vorticity.

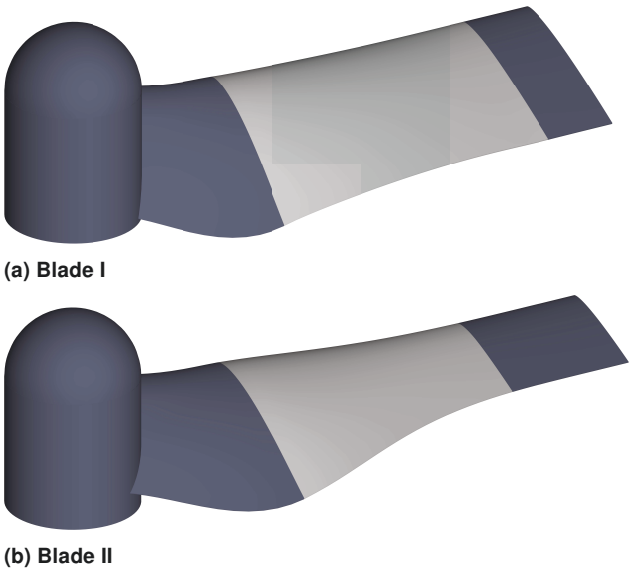

(a) Blade I

(b) Blade II

FIG 11. Schematic of the blade geometries obtained by the VFM inverse design method.

To obtain the velocity field, planar PIV measurements are performed using phase-triggered recording. A single camera (Imager sCMOS) with a resolution of 2048x2048 pixels is used for particle image acquisition. The flow is seeded with cubic polyamide particles of mean diameter 50 µm and a density of 1.016 g cm^{-3}, which are illuminated by a double-pulsed laser (Quantel Twins Ultra), providing a pulse energy of 120 mJ at an effective wavelength of 530 nm. In order to achieve a suitable vector resolution, the dimensions of the measurement plane are limited to 120x120 mm^2. Consequently, three overlapping *fields of view* (FOV) are recorded to capture the complete vortex sheet; compare figure 12. For each FOV, 400 frames are recorded to ensure statistical independence. Driven linear axes are used to precisely position the measuring plane closely behind the trailing edge of the blade.

5. RESULTS AND DISCUSSION

The obtained experimental data for both configurations in terms of the spanwise bound circulation distribution is presented in figure 13. A comparison to the design specification proves close agreement in the main blade section, both qualitatively and quantitatively, thus demonstrating the capability of the proposed method. It is evident that the agreement is significantly stronger when compared to the results of the BEMT [†].

Significant deviations are observed in close proximity to the rotor hub and near the blade tip, which are de-

[†]A conventional BEMT formulation with Prandtl's tip correction [12] is used for reference [8]. The convergence of the BEMT algorithm was improved based on a modified fixed point iterative method as proposed by Sun et al. [35].

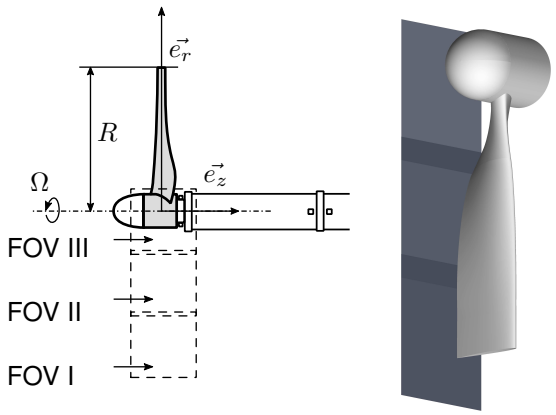

FIG 12. Position of the 2C-PIV measurement planes with respect to the rotor.

pendent on the considered blade configuration. In the case of the first blade, the spanwise circulation distribution is decreasing noticeably towards the blade tip in comparison to the theoretical prediction, whereas the spanwise circulation distribution in the second case is near constant and of predicted magnitude. Regarding the spanwise circulation distribution in the transition section, discrepancies can be recognised in both cases, although these are more prominent for Blade II. Within the scope of the potential theory, important limitations of the proposed VFM design method are as follows: First, the influence of the vortex sheet rollup is neglected by applying a prescribed wake model within the design method and thus disregarding the self-induced vortex sheet dynamics. Second, wake contraction is not modelled, as non-congruent but rigid helices represent the geometry of the vortex filaments. At last, the chordwise expansion of the rotor blade is not considered.

5.1. Decambering effect

Since the two configurations differ in their spanwise chord length distribution and the higher aspect ratio blade (Blade II) achieves a better representation of the predefined circulation distribution in the blade tip section, the chordwise expansion in the rotor plane may have the dominant influence on the observed deviations. In the present case, the VFM design method overestimates the loading in the proximity of the tip for both designs, which is in accordance with the findings of Soerensen et al. [22] on the influence of the chord distribution. To further investigate the case, an extended VFM approach (EVFM, see section 2.3) is employed, implementing a decambering correction to model the influence of chordwise expansion, as the conventional VFM model is limited to computing induced velocities in the rotor plane.
In the context of the following considerations, it is again to be noted that the VFM inverse design method is theoretically in exact consistency with the VFM analysis formulation. This statement also applies for the EVFM, when one assumes infinitesimal axial grid spacing and an infinite expansion of the grid from the rotor plane in the axial direction. In practical application, an interpolation method is applied to the pitch angle in the hub, transition, and tip region in order to gain a coherent solid body with adequate mechanical resistance, as specified in section 3.2. The latter leads to slight deviations, which are an order of magnitude smaller than the effects to be analysed.
The considered EVFM model uses rectangular singularities in a uniform helical mesh grid attached to the trailing edge, and the grid spacing in the axial direction is defined to be half the one obtained in the radial direction. The analysis is carried out based on LLT using a radial discretization of the rotor blade with 40 blade elements. The grid is generated utilizing the far wake helical pitch correlation (equation 18), evaluated using the azimuthally averaged induced velocity formulae (equation 27 and equation 28). The expansion of the grid in the axial direction is set to 20 rotations, whereas the decambering correction is implemented on the basis of a chord discretization with 25 nodes. In terms of additional corrections, the presented EVFM model is consistent with the VFM inverse design method, as the correction regime presented in section 3.2 is applied.
The results obtained within EVFM with decambering correction are given in figure 14 in comparison to VFM analysis and demonstrate a qualitatively closer agreement to the designated circulation distribution for the higher aspect ratio blade (Blade II). Hence, EVFM theoretical predictions support the hypothesis that the different characteristics of the circulation distribution in the blade tip section are attributed to the decambering effect.
It should be noted that the preceding considerations regarding the decambering effect are in principle applicable to BEMT [22]

6. CONCLUSIONS

A design methodology has been developed that enables rotor blade design on the basis of a targeted radial bound circulation distribution. The methodology relies on a VFM formulation for rotor wake modelling in combination with a LLT model of the rotor blade. Considering this approach, a VFM inverse design algorithm was presented along with a VFM analysis formulation. The latter was extended to a helical mesh model to take into account the influence of the chordwise expansion of the rotor blade and thus the resulting decambering effect.
Both propeller and wind turbine regimes were considered theoretically, while quantitative experimental validation was carried out on two example reference propeller configurations using planar PIV. The experimental results are in good agreement with theoretical predictions; however, deviations occur in the blade tip section that are differently pronounced and can be attributed to the decambering influence in the range of parameters considered. Consequently, it is advisable to take the decambering correction into account in the design process.

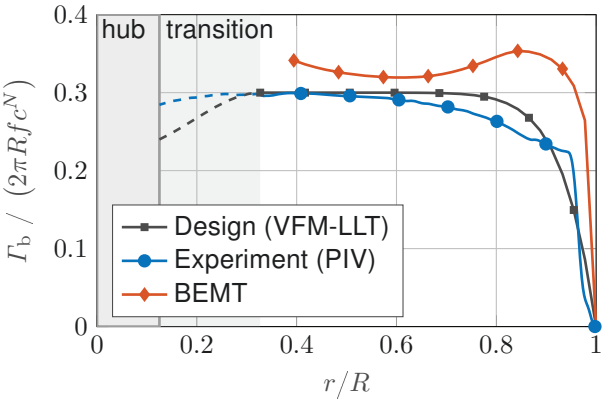

(a) Blade I

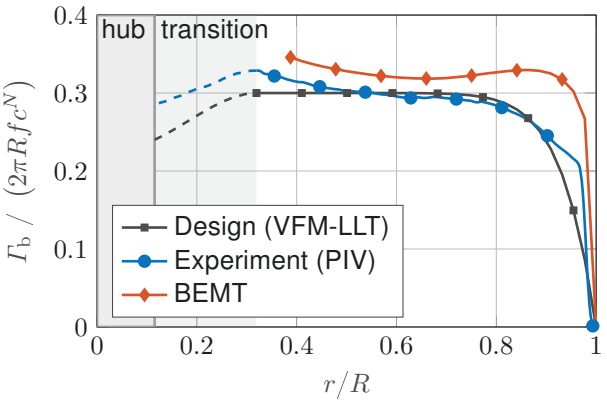

(b) Blade II

FIG 13. Comparison of experimentally obtained and targeted radial bound circulation distribution. BEMT results with Prandtl's tip correction are given for reference.

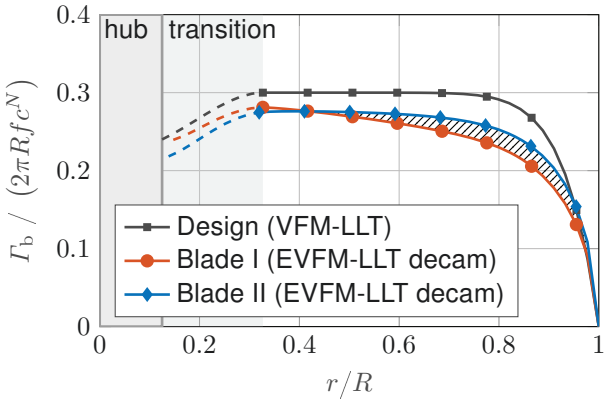

FIG 14. Comparison of radial bound circulation distribution obtained from VFM-LLT and EVFM-LLT with decambering correction.

The presented methodology is relevant in terms of the design specification of a certain load distribution and may be applied in a systematic approach to influence the vortex structures in the rotor wake.

Contact address:

niklas.pissarski@rwth-aachen.de

References

[1] Y. H. Yu. Rotor blade–vortex interaction noise. *Progress in Aerospace Sciences*, 36(2):97–115, 2000. DOI: 10.1016/S0376-0421(99)00012-3.

[2] R. Zhao, W. Shen, T. Knudsen, and T. Bak. Fatigue distribution optimization for offshore wind farms using intelligent agent control. *Wind Energy*, 15(7):927–944, 2012. DOI: 10.1002/we.1518.

[3] D. Schröder, T. Leweke, R. Hörnschemeyer, and E. Stumpf. Experiments on helical vortex pairs in the wake of a rotor. In *AIAA Scitech 2021 Forum*, Reston, Virginia, 2021. American Institute of Aeronautics and Astronautics. DOI: 10.2514/6.2021-1088.

[4] D. Schröder, J. Aguilar-Cabello, T. Leweke, R. Hörnschemeyer, and E. Stumpf. Experimental investigation of a rotor blade tip vortex pair. *CEAS Aeronautical Journal*, 13(1):97–112, 2022. DOI: 10.1007/s13272-021-00555-1.

[5] B. J. Bayly. Three-dimensional centrifugal-type instabilities in inviscid two-dimensional flows. *The Physics of Fluids*, 31(1):56–64, 1988. DOI: 10.1063/1.867002.

[6] P. Billant and F. Gallaire. Generalized rayleigh criterion for non-axisymmetric centrifugal instabilities. *Journal of Fluid Mechanics*, 542:365–379, 2005. DOI: 10.1017/S0022112005006464.

[7] P. Billant and F. Gallaire. A unified criterion for the centrifugal instabilities of vortices and swirling jets. *Journal of Fluid Mechanics*, 734:5–35, 2013. DOI: 10.1017/jfm.2013.460.

[8] J. N. Sørensen. *General Momentum Theory for Horizontal Axis Wind Turbines*, volume 4 of *Research Topics in Wind Energy*. Springer International Publishing, Cham, 2016. ISBN: 978-3-319-22113-7. DOI: 10.1007/978-3-319-22114-4.

[9] D. A. Peters and C. J. He. Correlation of measured induced velocities with a finite–state wake model. *Journal of the American Helicopter Society*, 36(3):59–70, 1991. DOI: 10.4050/JAHS.36.59.

[10] H. Glauert. Airplane propellers. In W. F. Durand, editor, *Aerodynamic Theory*, pages 169–360. Springer, New York, 1935. DOI: 10.1007/978-3-642-91487-4_3.

[11] W. Z. Shen, R. Mikkelsen, J. N. Sørensen, and C. Bak. Tip loss corrections for wind turbine computations. *Wind Energy*, 8(4):457–475, 2005. DOI: 10.1002/we.153.

[12] L. Prandtl. *Vier Abhandlungen zur Hydrodynamik und Aerodynamik*. Göttinger Nachrichten, Göttingen, 1927.

[13] A. M. Kuethe and J. D. Schetzer. *Foundations of Aerodynamics*. John Wiley & Sons, Inc., New York, 2nd edition edition, 1959.

[14] N. Ramos-García, J. N. Sørensen, and W. Z. Shen. Validation of a three-dimensional viscous–inviscid interactive solver for wind turbine rotors. *Renewable Energy*, 70:78–92, 2014. DOI: 10.1016/j.renene.2014.04.001.

[15] N. Ramos-García, A. Abraham, T. Leweke, and J. N. Sørensen. Multi-fidelity vortex simulations of rotor flows: Validation against detailed wake measurements. *Computers & Fluids*, 255, 2023. DOI: 10.1016/j.compfluid.2023.105790.

[16] V. L. Okulov and J. N. Sørensen. Optimum operating regimes for the ideal wind turbine. *Journal of Physics: Conference Series*, 75, 2007. DOI: 10.1088/1742-6596/75/1/012009.

[17] V. L. Okulov and J. N. Sørensen. An ideal wind turbine with a finite number of blades. *Doklady Physics*, 53(6):337–342, 2008. DOI: 10.1134/S1028335808060128.

[18] J. C. Hardin. The velocity field induced by a helical vortex filament. *The Physics of Fluids*, 25(11):1949–1952, 1982. DOI: 10.1063/1.863684.

[19] Emmanuel Branlard. *Wind Turbine Aerodynamics and Vorticity-Based Methods: Fundamentals and Recent Applications*, volume 7 of *Research Topics in Wind Energy*. Springer, Cham, 2017. ISBN: 978-3-319-55163-0.

[20] V. L. Okulov. The velocity field induced by vortex filaments with cylindric and conic supporting surface. *Journal of Engineering Thermophysics*, 5:63–85, 1995.

[21] H. Lerbs. Moderately loaded propellers with a finite number of blades and an arbitrary distribution of circulation. Technical Report T1952-1, Hamburgische Schiffbau Versuchsanstalt, Hamburg, 1952.

[22] J. N. Sørensen, K. O. Dag, and N. Ramos-García. A refined tip correction based on decambering. *Wind Energy*, 19(5):787–802, 2016. DOI: 10.1002/we.1865.

[23] J. Katz and A. Plotkin. *Low-speed aerodynamics: From wing theory to panel methods*. McGraw-Hill series in aeronautical and aerospace engineering. McGraw-Hill, New York, 1991. ISBN: 978-0070504462.

[24] W. F. Phillips and D. O. Snyder. Modern adaptation of prandtl's classic lifting-line theory. *Journal of Aircraft*, 37(4):662–670, 2000. DOI: 10.2514/2.2649.

[25] Mark Drela. Xfoil: An analysis and design system for low reynolds number airfoils. In T. J. Mueller, editor, *Low Reynolds Number Aerodynamics*, volume 54 of *Lecture Notes in Engineering*, pages 1–12. Springer, Berlin, Heidelberg, 1989. DOI: 10.1007/978-3-642-84010-4_1.

[26] H. Snel, R. Houwink, and J. and Bosschers. Sectional prediction of lift coefficients on rotating wind turbine blades in stall. Technical Report ECN-C-93-052, Energy Research Centre of the Netherlands, Petten, 1994.

[27] R. MacNeill and D. Verstraete. Blade element momentum theory extended to model low reynolds number propeller performance. *The Aeronautical Journal*, 121(1240):835–857, 2017. DOI: 10.1017/aer.2017.32.

[28] J. E. Kerwin and R. Leopold. A design theory for subcavitating propellers. *Transactions of the Society of Naval Architects and Marine*, page 72, 1964.

[29] V. G. Mishkevich. A new approach to lifting line theory: Hub and duct effects. *Journal of Ship Research*, 50(2):138–146, 2006. DOI: 10.5957/jsr.2006.50.2.138.

[30] H. Snel, R. Houwink, and W. J. Piers. Sectional prediction of 3d effects for separated flow on rotating blades. In *18th European Rotorcraft Forum*. 1992.

[31] C. Lindenburg. Investigation into rotor blade aerodynamics: Analysis of the stationary measurements on the uae phase-vi rotor in the nasa-ames wind tunnel. Technical Report ECN-C–03-025, Energy Research Centre of the Netherlands, Petten, 2003.

[32] C. Lindenburg. Modelling of rotational augmentation based on engineering considerations and measurements. Technical Report ECN-RX–04-131, Energy Research Centre of the Netherlands, Petten, 2004.

[33] Z. Du and M. Selig. A 3-d stall-delay model for horizontal axis wind turbine performance prediction. In *ASME Wind Energy Symposium*, Reston, Virigina, 1998. American Institute of Aeronautics and Astronautics. DOI: 10.2514/6.1998-21.

[34] P. K. Chaviaropoulos and M. O. L. Hansen. Investigating three-dimensional and rotational effects on wind turbine blades by means of a quasi-3d navier-stokes solver. *Journal of Fluids Engineering*, 122(2):330–336, 2000. DOI: 10.1115/1.483261.

[35] Z. Sun, W. Z. Shen, J. Chen, and W. J. Zhu. Improved fixed point iterative method for blade element momentum computations. *Wind Energy*, 20(9):1585–1600, 2017. DOI: 10.1002/we.2110.